Field surveying and numerical simulation of the Typhoon Hato storm surge event in Guangdong province, China

Xianwu Shi[1,2], Qichao Chen[1,2], Haoxuan Du[3], Ning Jia[4], Jian Fang[5], Mingli Zhao[6], Shan Liu[4]

[1] State Key Laboratory of Earth Surface Processes and Disaster Risk Reduction, Beijing Normal University, Beijing, 100875, China
[2] Key Laboratory of Environmental Change and Natural Disaster, Ministry of Education, Beijing Normal University, Beijing, 100875, China
[3]State Key Laboratory of Internet of Things for Smart City and Department of Ocean Science and Technology, University of Macau, Macao, People's Republic of China
[4] National Marine Hazard Mitigation Service, Beijing 100194, China
[5] College of Urban and Environmental Sciences, Central China Normal University, Wuhan, 430079, China
[6] South China Sea Marine Institute of Environmental and Planning, State Oceanic Administration, Guangzhou, 510310, China

Correspondence to: Shan Liu (liu_shan123@126.com)

Abstract. In 2017, Typhoon Hato hitting Zhuhai city, Guangdong province, caused a severe storm surge disaster. In this study, a systematic field survey of the "Hato" storm surge was conducted and the numerical modeling of inundation extent and depth was performed. The survey integrated floating debris tracking, inundation tracing, and local inquiries to determine the seawater inundation edge points, water depths, and overall extent of the flooding. Combined with field reconnaissance, the mechanisms damaging typical hazard-bearing bodies during marine disasters were clarified, and the effects of the "Hato" storm surge were analyzed. Inundated areas were distributed in coastal cities, with the maximum inundation depth up to about 2 m, and the inundated area exceeding 54.08 km^2. Compared to historical storm surge records, Typhoon Hato ranked as the fourth most severe and stands as one of the most devastating storm surges to impact Guangdong province over the past decade. In addition, the proposed model can reproduce this typhoon and storm surge event, which was evaluated by comparing field observations with numerical simulations, showing good consistency with the observed flooding records. These results could provide detailed data and decision support, which can be used as guidance for the mitigation of future storm surges in coastal areas.

1 Introduction

Coastal flooding induced by tropical cyclones is among the most destructive marine hazards worldwide and poses an increasing threat to densely populated coastal regions (Feehan et al., 2024). Under the combined influence of climate change, accelerated sea-level rise, rapid urbanization, and the growing exposure of coastal infrastructure, storm surge disasters are becoming increasingly frequent and severe, resulting in substantial losses of human lives, economic assets, and ecosystem services (Guo et al., 2023; Zhang et al., 2026). In low-lying estuarine regions, storm surge hazards are often further amplified by complex interactions among astronomical tides, river discharge, coastal geomorphology, and local topography, producing extensive inundation with highly heterogeneous spatial characteristics (Du et al., 2024b). Consequently, accurately characterizing storm surge inundation processes and their impacts has become a fundamental prerequisite for improving coastal flood modelling, disaster risk assessment, and climate adaptation strategies. As one of the countries most frequently affected by tropical cyclones, China experiences severe storm surge disasters almost every year, particularly along the southeastern coast, where densely populated urban agglomerations and rapidly expanding coastal economies are highly vulnerable to extreme marine hazards (Shi et al., 2015, 2020).

Over the past two decades, considerable progress has been made in understanding storm surge processes through numerical modelling, remote sensing observations, and post-event field investigations (Gharehtoragh and Johnson, 2024; Vogt et al., 2024; Zhang and Zhang, 2024). Hydrodynamic models have been widely applied to simulate storm surge propagation and coastal inundation under historical and future climate scenarios, providing valuable tools for storm surge prediction and risk assessment (Passeri et al., 2018). Furthermore, Satellite remote sensing has also significantly enhanced the capacity for rapid, large-scale identification of inundated areas following extreme events (Khan and Basalamah, 2023). However, both approaches have inherent limitations. Numerical simulations are affected by uncertainties associated with topography, boundary conditions, model parameterization, and the representation of urban infrastructure. While high-resolution optical imagery is constrained

by satellite revisit frequency, image availability, and spatial resolution, and primarily provides information on inundation extent rather than maximum inundation depth or field evidence such as flood marks and damage characteristics required for comprehensive disaster assessment and model validation (Cao et al., 2023; Muis et al., 2023). In contrast, post-event field investigations provide irreplaceable first-hand information on flood marks, inundation extent, water depth, debris distribution, infrastructure damage, and eyewitness observations, making them indispensable for understanding disaster processes and validating numerical simulations (Widiyanto et al., 2019).

Previous post-event field investigations have substantially improved the understanding of storm surge inundation characteristics and disaster impacts, several gaps remain. First, uncertainties associated with field-based evidence reconstruction have not been sufficiently addressed, despite the fact that inundation boundaries and flood depths are often derived from indirect indicators such as floating debris, vegetation damage, seawater traces, and local interviews (Bösmeier et al., 2022). Furthermore, while numerical models have become important tools for storm surge simulation and coastal flood risk assessment, the potential of field observations as benchmark datasets for model validation has not been fully exploited (Jiao et al., 2025). Limited integration between comprehensive post-event observations and numerical simulations may constrain the evaluation of model reliability and the improvement of coastal flood prediction. Therefore, integrated approaches combining field surveys, disaster mechanism analysis, and numerical model validation are still needed to better understand towards storm surge impacts and enhance coastal flood risk assessment.

This study conducted a systematic post-event field investigation of the storm surge induced by Typhoon Hato in Guangdong Province. The objectives were to: (1) characterize the spatial distribution and inundation characteristics of the storm surge using field reconnaissance, RTK measurements, inundation tracing, and interviews; (2) investigate the damage mechanisms of representative hazard-bearing bodies and analyze the regional disaster impacts; and (3) evaluate the capability of a previously developed numerical model to reproduce observed water-level dynamics and inundation characteristics, including inundation extent and depth, by integrating tidal-station observations with post-event field surveys. By integrating large-scale field investigations with numerical model validation, this study provides valuable evidence for improving storm surge disaster assessment, enhancing confidence in coastal flood simulations, and supporting future coastal disaster prevention and risk management.

2 Materials and methods

2.1 Study area and data

Typhoon Hato (No. 13) formed over the northwestern Pacific Ocean at 14:00 on August 20, 2017 (local time). Its intensity continuously increased, and it became a severe tropical storm by 08:00 on August 22 and changed to a typhoon at 15:00 with maximum wind speed exceeding 25 m/s. “Hato” finally became a severe typhoon at 07:00 on August 23 and made landfall on the coast near to the Jinwan District of Zhuhai City, Guangdong province, at 12:50. During the landfall (Fig. 1), the maximum wind speed reached 45 m/s, and the lowest pressure at the center was 950 hPa. After making landfall near Zhuhai in the Pearl

River Delta, Hato generated an extreme storm surge that coincided with high astronomical tide, causing widespread coastal inundation and severe socioeconomic losses throughout Guangdong Province. The maximum storm wave height was recorded over 8 m at an offshore station. The National Marine Forecasting Center released an orange alert with respect to the storm surge and a red-alert with respect to waves on August 22. Affected by the typhoon, a conspicuous storm surge occurred along the coast from eastern Guangdong to Yangjiang. Typhoon Hato (2017) provides an ideal case for investigating storm surge inundation characteristics and evaluating numerical model performance in a highly urbanized estuarine environment. The Pearl River Delta is characterized by a highly urbanized coastline, complex estuarine geomorphology, dense river networks, and extensive coastal infrastructure, making it one of the regions most vulnerable to storm surge disasters in China (Qiu et al., 2022; Wang et al., 2021). The large spatial extent of the affected area and the availability of comprehensive post-event field observations provide a valuable opportunity to investigate regional inundation characteristics and assess the reliability of numerical storm surge simulations.

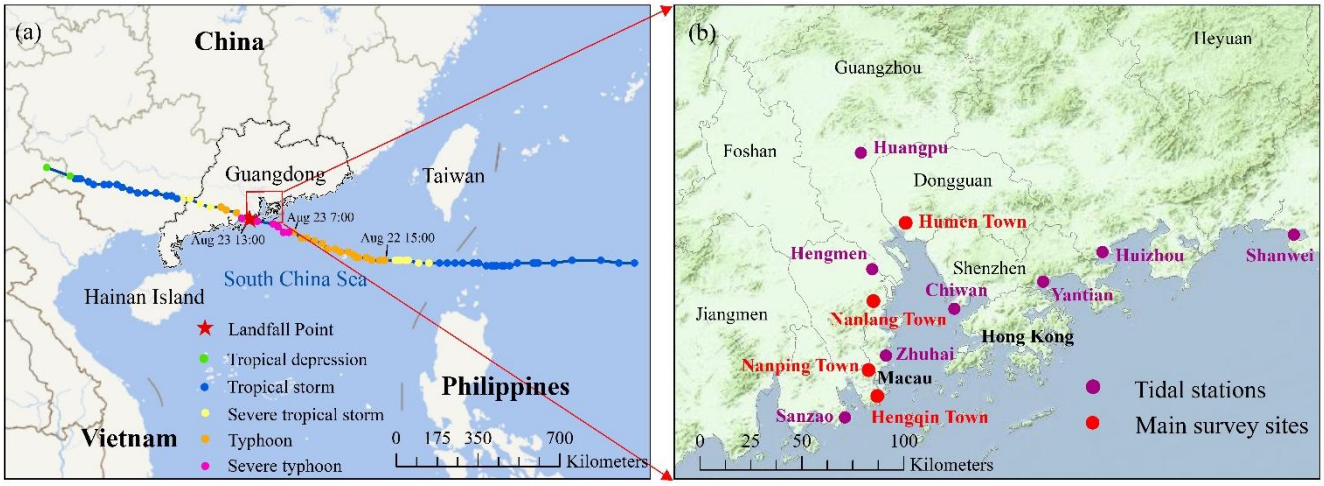


Figure 1. (a)Track and intensity variation of Typhoon Hato. (b) The spatial distribution of tidal stations (purple circles) and main field survey sites (red circles).

This study focused on Guangdong province influenced by “Hato” and the induced storm surge. Guangdong province has a coastline of 4,114 km which includes 14 coastal cities. Guangdong province is one of the provinces where the most serious marine disasters occur. In the past decade (2011 to 2020), the average direct economic loss owing to marine disasters in Guangdong province was 2.8 billion yuan. Many places in Guangdong were inundated to varying degrees, resulting in severe losses by “Hato” storm surge. Based on the statistics, more than 1 million people in the Guangdong province were affected by the disaster, and six people died. The typhoon storm surge affected 18,238.80 ha of aquaculture (>10% loss). It caused the losses of 22,800 t of aquaculture output and 330 sets of aquaculture equipment and facilities, as well as damaged 275 fishing vessels, 240.18 km of groins, and 532.08 km of seawalls and revetments (Guangdong Provincial Department of Oceans and

Fisheries, 2018). This study analyzes the influence of typhoon "Hato" storm surge. Additionally, multisource data were collected in this study (Table 1).

Table 1. Multisource data collected in this study

Data type	Time series	Description	Source
Historical typhoon records	1949–2025	Time, location, and intensity of each typhoon track point	Shanghai Typhoon Institute, China Meteorological Administration
Historical storm surge loss data	1990–2025	Loss data including economic, death, and building destroyed	National Marine Mitigation Service
Tidal observational data	1990–2025	Hourly observational data of surge and water level for tidal station during typhoon periods	South China Sea Marine Forecasting Center, Oceanic Administration of China
National Gross Ocean Product	2017	The value of National Gross Ocean Product in Guangdong Province	State Oceanic Administration of China

2.1.1 Numerical simulation

The numerical simulation results used in this study were derived from an integrative compound flood modelling framework developed by Du et al. (2024a), which was applied to reproduce the extreme compound flood event induced by Typhoon Hato (2017) in the Pearl River Delta (PRD) (Fig. 2). The framework integrates coastal, fluvial, and pluvial flood processes within a unified two-dimensional hydrodynamic modelling system, allowing the interactions among storm surge, astronomical tide, rainfall, and river discharge to be represented simultaneously. The core of the framework is a two-dimensional depth-averaged hydrodynamic model based on unstructured triangular meshes. The model solves the shallow water equations with additional source terms representing rainfall forcing, atmospheric pressure gradients, and wind shear stresses, enabling the simulation of compound flooding processes induced by tropical cyclones. The model is driven by multiple forcing datasets, including astronomical tidal constituents from the TPXO9 global tidal model, typhoon-induced wind and atmospheric pressure fields reconstructed from official typhoon track data, rainfall forcing from the Weather Research and Forecasting (WRF) model, and river discharge simulated by the CREST distributed hydrological model. The model provides spatially continuous inundation depth and water-level outputs throughout the typhoon lifecycle. In the original study, the model performance was evaluated using multiple observational datasets, demonstrating its capability to reproduce the hydrodynamic processes and compound flood characteristics associated with Typhoon Hato. In this study, simulated water levels were compared with hourly observations from four tidal stations, while simulated inundation extents and depths were evaluated against post-event field survey observations to assess the performance of the numerical model.

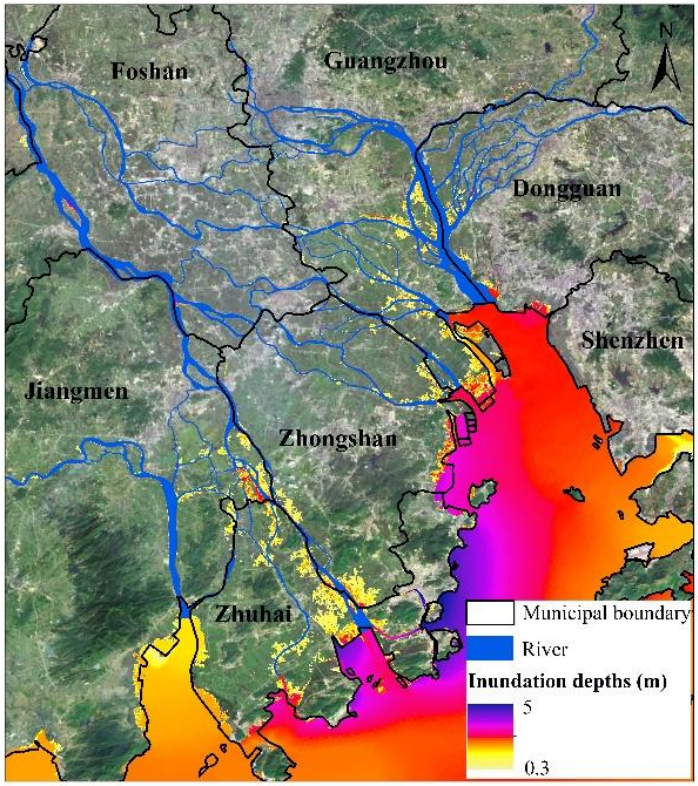


Figure 2. Simulated storm surge inundation depth distribution caused by Typhoon Hato in the Pearl River Estuary.

For the Typhoon Hato simulation, the computational domain covered the South China Sea, the East China Sea, and the western North Pacific, together with the Pearl River Delta and its major river systems. An unstructured mesh was adopted, with spatial resolution gradually refined from approximately 10 km in the deep ocean to 50 m in the delta and river system, and to 5 m over the Macau Peninsula. The model was forced by astronomical tides at the open-ocean boundaries and river discharge at the upstream boundaries, while typhoon-induced wind and atmospheric pressure fields and rainfall were applied as time-varying forcings. The simulation covered the entire Typhoon Hato event, from 00:00 UTC on 20 August to 00:00 UTC on 25 August 2017. Manning roughness coefficients were set to 0.016 for the deep sea, 0.025 for offshore areas, and 0.040 for land . A critical water depth of 0.1 m was adopted to control the wetting and drying processes. Wave effects were not considered because previous studies reported a limited influence of waves on storm-surge inundation in the Pearl River Delta.

2.2 Investigation of Damage to exposures

Mariculture areas, fishing ports, and coastal dike are the most severely affected by storm surge. In this study, the disaster-causing mechanisms and damage to typical hazard-bearing bodies affected by storm surge were analyzed using visual

interpretation, field measurements, and field reconnaissance. The damage to the mariculture area is mainly reflected in the death and damage of the aquaculture and the aquaculture facilities affected by the disaster. Through on-site inquiries, the damages to different types of aquaculture and aquaculture facilities, the sales price of the aquaculture and the purchase price of the aquaculture facilities were recorded, and the damage to the marine aqua-culture industry was calculated. The damage to the fishing port is reflected in the loss caused by the collision of fishing boats in the port area affected by the disaster. Through field surveys, the number and extent of damage to different types of fishing boats were counted, and the cost and repair prices of different types of fishing boats were understood. To identify the extent of damage to the coastal dike, the basic conditions of the embankment engineering construction standards, construction materials, etc., the length of the damage (using tape measure and laser rangefinder) were investigated. During field reconnaissance, photos were obtained using far and near angles. At least six photos of a single characteristic point were obtained to completely reflect the location and degree of damage to disaster-bearing bodies (Fig. 3).

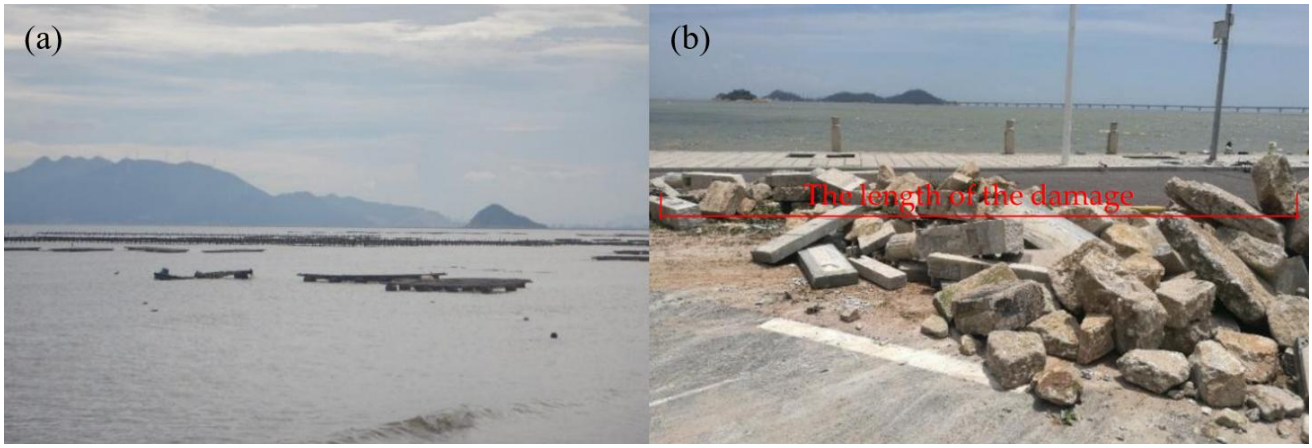


Figure 3. (a) Damaged aquaculture fish rafts in Mutouchong village, Zhuhai city. (b) Damage length of the guardrail along the Qinglu Middle Road in Zhuhai city (~50 m).

2.3 Inundation Investigation

To quantify the water depth and inundation areas caused by storm surge, the survey of the submerged area generally involves three methods: searching for drifting objects, identifying residual inundation traces, and conducting interviews with local residents. In this study, these complementary methods were jointly used to assess the reliability of the reconstructed storm-surge inundation extent (Table 2). First, inundation edge points were identified based on multiple field indicators, including the accumulation of floating objects, such as dead tree branches transported to the edge of inundated areas, information provided by coastal residents regarding whether inundation occurred, and residual inundation traces on coastal buildings. To reduce subjectivity in the interpretation of these field indicators, their reliability was assessed according to both the estimated vertical uncertainty and the degree of independent corroboration. Evidence with a vertical uncertainty of ≤0.10 m was classified as reliable when the inundation trace was clearly identifiable and supported by at least two independent indicators or cross-

checked by multiple investigators or respondents. Evidence with a vertical uncertainty of >0.10–0.20 m was classified as less reliable, whereas evidence with a vertical uncertainty of >0.20 m or without a reasonably quantifiable uncertainty was classified as reference only. These thresholds were adopted as operational criteria for this study, following established practices for evaluating uncertainty and reliability in post-event high-water-mark surveys (Dottori et al., 2013; Feaster and Koenig, 2017; Koenig et al., 2016). Similar multi-level reliability assessment approaches have been applied in recent post-event tsunami surveys by considering measurement accuracy, cross-checking, and field conditions (Yuhi et al., 2024). After the edge points were determined, their longitude, latitude, and elevation were measured using RTK and other surveying techniques (Fig. 4). Based on the positions of the edge points, plane survey grids were established. Survey grids were densely distributed in coastal areas containing residential areas, schools, ports, and aquaculture facilities, with the distance between adjacent survey points generally less than 300 m. The investigation team determined inundation depth by measuring residual inundation traces in inundated residential areas and recorded the observations in a storm-surge inundation survey form. Finally, interviews with local residents were conducted to further cross-check and revise the reconstructed inundation extent and depth.

Table 2. Determination of the reliability of the storm surge inundation investigation.

Reliability level	**Quantitative criteria**	**Field-evidence criteria**
Reliable	Vertical uncertainty ≤ 0.10 m	Clearly identifiable field evidence, supported by at least two independent indicators or cross-checked by multiple investigators/respondents
Less reliable	0.10 m < vertical uncertainty ≤ 0.20 m	Directly observed or reported evidence with limited independent corroboration, incomplete traces, or local ambiguity
Reference only	Vertical uncertainty > 0.20 m, or uncertainty cannot be reasonably determined	Indirect information, personal recollection, or ambiguous traces without sufficient independent corroboration



Figure 4. Example of topographic tools and techniques used for flood range measure. (a) and (b) location of flood range using RTK, (c) and (d) determination of flood height or water depth during flood using a measure tape.

3 Results and Analysis

3.1 Analysis of Disaster Causes

This disaster caused serious damage to the human lives, vehicles, fishery, vessels, coastal structures, and other hazard-bearing bodies in the Guangdong province. The main causes of damage to these hazard-bearing bodies were identified using field reconnaissance:

First, the storm surge caused the seawater to come ashore, inundating residential buildings along the coast, garages, lower-floor shopfronts, cars parked on the roadside, and aquaculture areas, causing suffocation and drowning of people as well as the loss of indoor properties, vehicles, and aquaculture products. Second, the combination of the storm surge and nearshore waves had a significant impact on coastal embankments, deep-water net cages, aquaculture rafts, and fishing vessels, resulting

in the damage to embankment surfaces, corners of embankment facilities, aquaculture facilities, and fishing vessels (due to collisions) as well as the death of aquaculture products due to collisions. A detailed description of the main causes of damage to various hazard-bearing bodies is shown in Table 3.

Table 3. Causes of damage to various exposed structures

Exposed structures		Damage causes
Human lives		• Underground garages were flooded, causing the drowning of people.
Fishery	**Pond culture**	• Facilities associated with coastal aquaculture ponds, such as board room, were destroyed by the storm surge. • Products from aquaculture suffered from hypoxia and died due to the lack of electricity to supply oxygen to the ponds because many power and oxygen supply facilities were damaged. • Many fish and shrimp swam away from fishponds when the water overflowed.
	Raft culture	• Fish breeding rafts for coastal raft cultures were washed away or dispersed by the storm surge and nearshore waves.
	Fishing boat	• Fishing vessels were turned over by nearshore waves, that is, coastal inundation. • Under the combined impact of the storm surge and nearshore waves, many fishing vessels crashed into docks, revetments, and seawalls and were damaged. • Fishing vessels were washed to the shore by the storm surge and nearshore waves and stranded.
Coastal structures	**Wharf**	• Under the impact of nearshore waves, the water-facing sides of wharves were damaged. • Many wharves were hit and damaged by merchant vessels under the impact of the storm surge and nearshore waves.
	Breakwater	• The storm surge and nearshore waves led to the failure of the protective sides and embankment roots.
	coastal dikes	• Bricks, rubble, and masonry at the bottom of revetments were washed away when the water-facing side was hit by the storm surge and nearshore waves. Thus, revetments were damaged.
House		• Walls and roofs of houses were damaged by the impact of nearshore waves. • Indoor property was damaged due to seawater immersion. • Temporary board room were destroyed by the storm surge.

Coastal Tourism Zone	• The coast and beach of lidos were filled with garbage and rocks washed ashore by the flood. • Signs, lighthouses, and other facilities of the lidos were destroyed by the storm surge and nearshore waves. • The office buildings of the lidos were flooded, and equipment failed to work properly. • The soil was exposed because the beach sand was swept away by the storm surge and nearshore waves, preventing the normal operation of the lidos.
Transportation	• Vehicle engine circuit systems were damaged due to seawater immersion and thus possibly scrapped. • Under the combined impact of the storm surge and nearshore waves, vehicles parked along the coast were swept out to sea and thus damaged. • Many vehicles were also damaged by falling branches and billboards.
Public facilities (e.g., electricity and communication facilities)	• Several facilities in low-lying areas were flooded and thus damaged.

3.2 Analysis of the Disaster Characteristics

Typhoon Hato hit the mouth of the Pearl River. The powerful typhoon pushed the sea water inward from the horn, and the sea water spread to the river network area. The maximum storm surge occurred 1–2 h after the astronomical high tide of the day. Thus, the peak storm surge was superimposed on the astronomical tide, resulting in a substantial increase in water levels near the Pearl River Estuary and evident exceedance of the warning water level. The high-tide levels at the Huizhou, Yantian, Chiwan, Huangpu, Hengmen, and Zhuhai stations in the Guangdong province exceeded the local red-alert tidal levels and the historical highs recorded at the stations (Table 4). Compared with the processes of catastrophic marine disasters of the past decade, the sea-level rise caused by Hato marine disaster was relatively significant, ranking fourth, higher than the average value of 3.663 billion yuan, and accounted for 0.066% of National Gross Ocean Product in 2017.

Table 4. Maximum storm surge residual and tidal levels at each tidal station during Typhoon Hato on August 23.

Observation station (point)		**Maximum storm surge**		**Maximum tide level**		**Warning water level (m)**
		Time	**Storm surge residual (m)**	**Time**	**Tidal level (m)**	
1	Huizhou	10:00	1.20	10:24	4.45	4.40 (Red)

2	Chiwan	13:00	2.03	12:51	5.59	4.87 (Red)
3	Yantian	10:00	1.29	09:44	4.21	4.12 (Red)
4	Huangpu	16:00	1.94	15:00	2.73	2.61 (Red)
5	Hengmen	14:00	2.15	14:00	2.94	2.36 (Red)
6	Zhuhai	12:00	2.79	12:00	6.14	4.67 (Red)
7	Sanzao	13:00	2.16	13:00	2.48	2.26 (Orange)
8	Shanwei	12:00	1.18	11:49	3.04	2.97 (Yellow)

Based on the field survey and disaster statistics, this storm surge seriously affected seven cities in the Guangdong province, such as Guangzhou, Zhuhai, Shenzhen, Dongguan, Zhongshan, Jiangmen, and Huizhou, and led to direct economic losses of 5.154 billion yuan (Table 5). The direct economic loss was the highest in Zhuhai of 4.401 billion yuan, accounting for 85% of the total direct economic loss. Table 7 shows that the population affected by the Typhoon Hato storm surge accounts for 65.8% of the annual disaster-affected population in the Guangdong province. The number of dead people accounts for 100% of the annual typhoon-related deaths, and the disaster-affected aquaculture area accounts for 74.7% of the annual affected area. The length of damaged coastal structures accounts for 99.5% of the length of the annual damaged coastal structures, the number of damaged vessels accounts for 76.8% of the annual damaged vessels, and the direct economic losses account for 96.1% of the annual direct economic losses(Table 6). The direct economic losses caused by the Hato marine disaster are higher than those due to marine disasters of the past decade (≳1 billion yuan), ranking fourth, and higher than the average value of 3.663 billion yuan.

Table 5. Analysis of the main disaster indicators.

City	Disaster-affected population (people)	Death (including missing; people)	Disaster-affected aquaculture area (ha)	Damaged coastal structures (km)	Sunk vessels (vessels)	Damaged fishing vessels (vessels)	Direct economic losses (10,000 yuan)
Guangzhou	43,500	0	2,337.99	0.62	0	0	11,235
Zhuhai	750,357	2	81.59	2.6	36	152	440,143
Jiangmen	291,070	4	5,558.5	0.08	7	42	30,762.1
Zhongshan	36,300	0	4,329.0	0	0	9	27,781.1
Shenzhen	—	0	—	1.96	0	11	3,737
Dongguan	7,421	0	4.69	0	0	0	101
Huizhou	—	0	5,927.0	767	0	18	1,665.2

Total	1,128,648	6	22,848.55	772.26	43	232	515,424.4

Note: "—" indicates no statistics.

Table 6. Comparison between the losses due to the Typhoon Hato and those caused by other typhoon storm surges that occurred throughout the year.

Index	Typhoon storm surges of the whole year	Typhoon Hato	Proportion (%)
Disaster-affected population (10,000 people)	171.46	112.86	65.8
Dead population (people)	6	6	100.0
Disaster-affected aquaculture area (1000 ha)	24.42	18.24	74.7
Length of damaged coastal structure (km)	776.01	772.26	99.5
Number of damaged vessels	358	275	76.8
Direct economic losses (100 million yuan)	53.61	51.54	96.1

3.3 Inundation

Based on the above-mentioned inundation survey methods, the cities Guangzhou, Zhuhai, Shenzhen, Zhongshan, Jiangmen, and Dongguan as well as other places in the Guangdong province were inundated to varying degrees. The seawater inundation was mainly caused by dike overflow, dike breach, and piping inundation. Based on the statistics, 13 townships in the Guangdong province were affected by the storm surge, resulting in 19 inundated sites with an accumulated inundated area exceeding 54.08 km^2. Inundated areas were mainly distributed in the Panyu, Huangpu, and Nansha districts of Guangzhou city; Xiangzhou District of Zhuhai city; Bao'an, Yantian, and Longgang districts of Shenzhen city; Nanlang Town of Zhongshan city; Guanghai, Duhu, and Chixi towns of Taishan, a county-level city of Jiangmen city; and Hongmei and Humen towns of Dongguan city (Table 7). In Zhuhai city, mainly the urban areas were in-undated. Passenger docks, office buildings, shops, and residential areas along the coast near to Qinglu Road, Xiangzhou District, were heavily inundated by seawater, with a maximum inundation depth of 2 m. Underground garages in several coastal communities were severely inundated, resulting in deaths. The most severe seawater inundation occurred in Jiangmen city. The inundated region mainly included mariculture area with a maximum inundation depth of 1 m and inundation extent of 24.75 km^2.

Table 7. Main inundation status in the survey area in the Guangdong province.

No.	Inundated area		Inundation type	Submergence depth (m)
1	Zhuhai	Xiangzhou District	Overflow dike	1.0–2.0
2		Hengqin Town	Overflow dike	0.3–0.8
3		Nanping Town	Overflow dike	0.3–0.8
4	Shenzhen	Bao'an District	Overflow dike	0.3–0.9
5		Yantian District	Overflow dike and dike breach	1.2–2.0
6		Longgang District	Overflow dike and dike breach	0.1–0.5
7	Guangzhou	Panyu District	Overflow dike	0.5–0.6
8		Huangpu District	Overflow dike	0.4–0.5
9		Nansha District	Overflow dike	0.5–0.6
10	Zhongshan	Nanlang Town	Overflow dike and floodplain	0.5–0.6
11	Jiangmen	Taishan (county-level city)	Overflow dike and dike breach	0.2–1.0
12	Dongguan	Humen Town	Overflow dike and piping	1.2–1.4
13		Hongmei Town	Overflow dike and piping	0.8–0.9

3.4 Model Validation

Field surveys provided valuable information on determining the spatial inundation range and depth distribution caused by storm surge. However, field observations mainly represent discrete locations and reconstructed inundation boundaries, whereas numerical models can provide spatially continuous estimates of inundation patterns. In this study, the simulated inundation results were further compared with field-derived inundation information to evaluate the capability of the numerical model in reproducing the flooding characteristics.

3.4.1 Water-level validation

To quantitatively evaluate the performance of the hydrodynamic model in reproducing the temporal evolution of water levels during Typhoon Hato, simulated water levels were compared with hourly observations at four tidal stations (Figure 5). Overall, the simulated and observed water levels showed a strong linear correspondence across all stations, with coefficients of determination (R^2) ranging from 0.895 to 0.948. The relatively high R^2 values indicate that the model successfully captured

the temporal variability of water levels during the event, including the overall rising and falling patterns associated with tidal fluctuations and storm induced water level changes. The magnitude of the errors was generally moderate, with RMSE values ranging from 0.164 to 0.310 m and MAE values ranging from 0.111 to 0.236 m. The best agreement was obtained at Zhuyin, where the model achieved an R^2 of 0.895, an RMSE of 0.164 m, and an MAE of 0.111 m, while Chiwan showed the highest R^2 (0.948) and relatively low errors (RMSE = 0.181 m; MAE = 0.147 m). Sishengwei exhibited the largest deviations, with an RMSE of 0.310 m and an MAE of 0.236 m, suggesting greater uncertainty in reproducing the local water-level response. At Hengqin, the regression slope was slightly greater than unity (1.060), indicating a modest amplification of the simulated water-level variability relative to the observations, whereas the slopes at the other three stations were slightly below unity (0.958–0.964), suggesting a generally consistent but slightly compressed response amplitude. The close correspondence between simulated and observed water levels across the four stations demonstrates that the model reasonably reproduces the hydrodynamic response to Typhoon Hato and provides a reliable basis for subsequent assessment of inundation extent and depth. The model performance was therefore further evaluated by comparing the simulated inundation extent and depth with field observations.

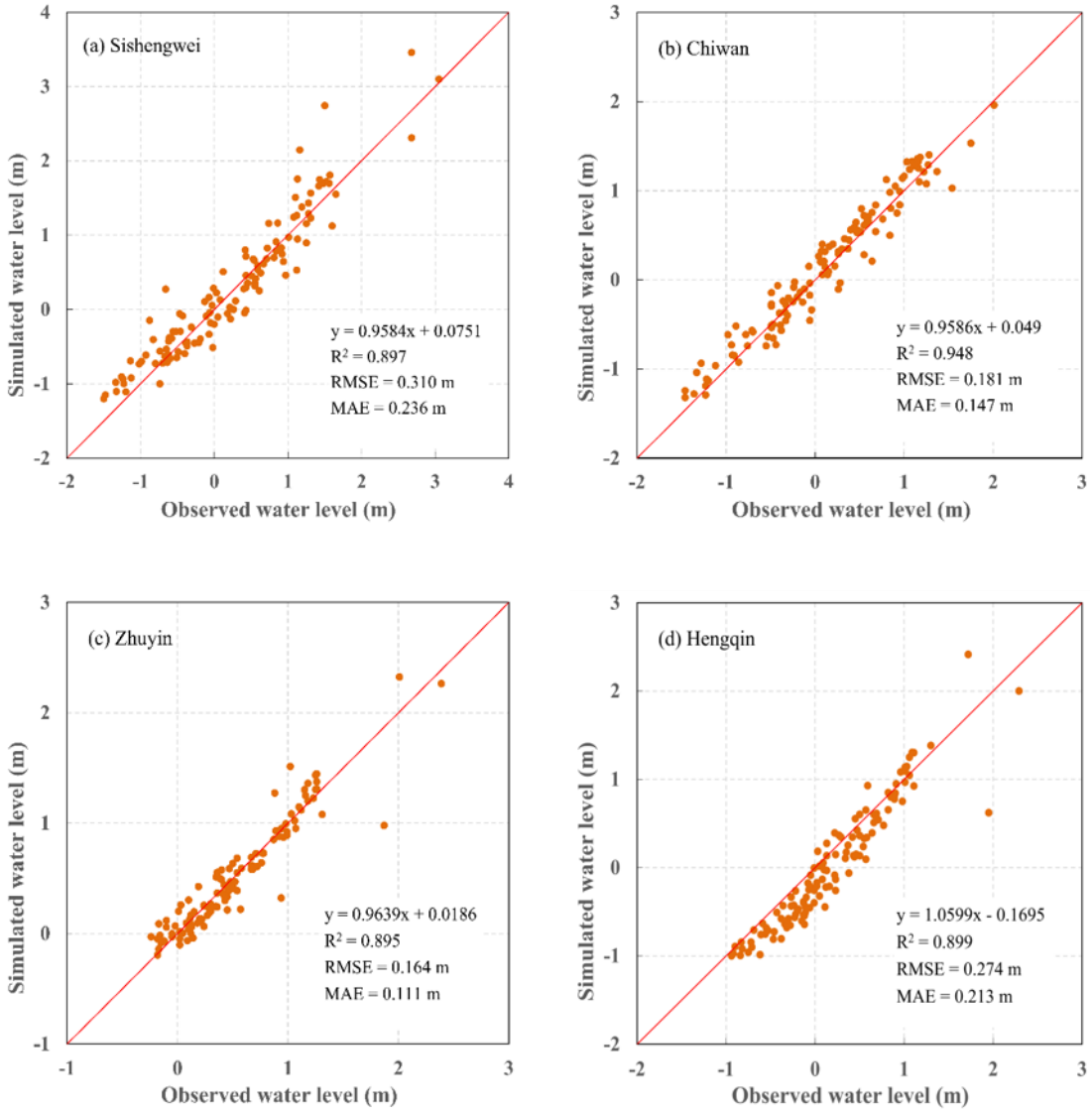


Figure 5. Comparison between the simulated and observed water levels during Typhoon Hato from 0:00 on August 20 to 0:00 on August 25. The red solid line denotes the 1 : 1 line.

3.4.2 Inundation extent and depth validation

The simulated and observed inundation extents were presented in Figure 6, which could be found that the numerical model successfully reproduced the major spatial patterns of storm surge inundation during Typhoon Hato. The simulated inundation areas were primarily distributed along low-lying coastal zones, estuarine regions, and areas adjacent to river networks, which were consistent with the inundation characteristics identified through post-event field surveys. A high degree of spatial consistency was observed between the simulated and field-observed inundation areas in several severely affected coastal regions, particularly Panyu District, Nanlang Town and Nansha District. In these areas, most of the observed inundated zones were located within or adjacent to the simulated inundation extents, indicating that the model effectively captured the dominant pathways of storm surge propagation and coastal flooding. Some differences were concentrated along coastal margins and complex land-water interaction regions, which may reflect the difficulties of resolving complex coastal environments such as small-scale topography, coastal protection works, and local hydrodynamic processes.

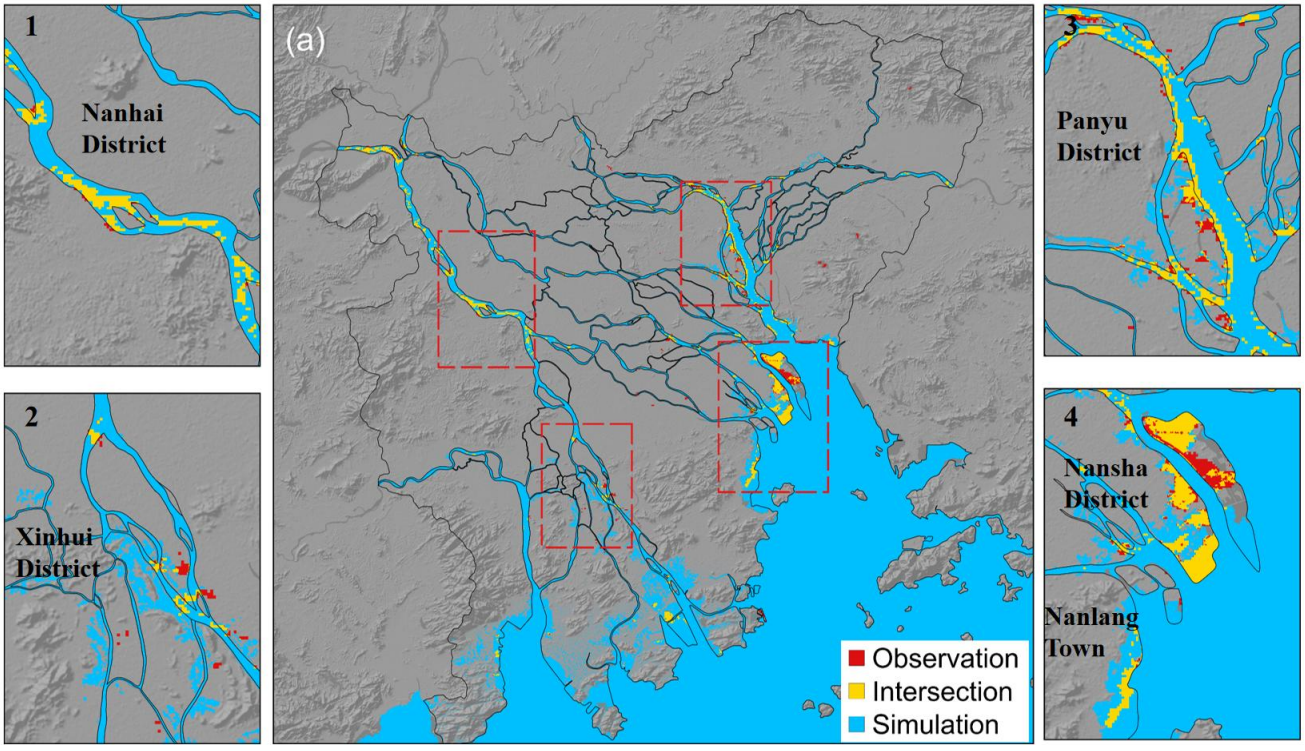


Figure 6. Comparison of field-observed and model-simulated storm surge inundation extents during Typhoon Hato. The red areas represent observed inundation boundaries derived from post-event field surveys, the blue areas indicate simulated

inundation extents from the numerical model, and the yellow areas show the spatial overlap between observations and simulations. Subfigures 1–4 provide enlarged views of representative inundated areas, allowing a detailed comparison between the observed and simulated inundation extents.

To further evaluate model performance, simulated inundation depths were extracted from representative inundated areas and compared with the depth ranges obtained from post-event field surveys (Figure 7). Overall, the simulated inundation depths showed good agreement with the surveyed depth ranges in most representative inundated areas, particularly in Hongmei, Humen, Nanping, Hengqin, Taishan, and Xiangzhou, where the median and mean simulated depths closely matched the field observations. The majority of simulated inundation depths fell within or close to the surveyed depth ranges, demonstrating that the numerical simulation successfully reproduced the overall flooding characteristics associated with Typhoon Hato.

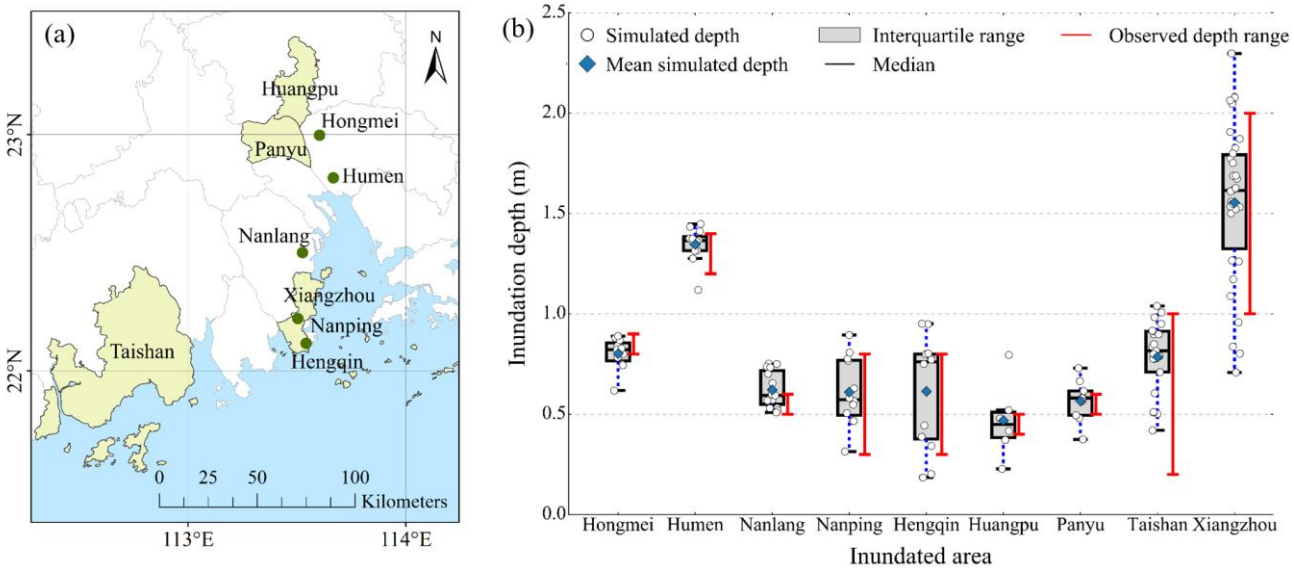


Figure 7. Validation of simulated inundation depths against post-event field observations in nine representative inundated areas affected by Typhoon Hato. (a) Locations of the representative validation areas in Guangdong Province. (b) Comparison between simulated inundation depths and observed inundation depth ranges. The boxplots summarize the distribution of simulated inundation depths extracted from validation points within each inundated area, where the box indicates the interquartile range (IQR), the horizontal line represents the median, the blue diamond denotes the mean simulated depth, and the circles represent individual simulated values. Red error bars indicate the observed inundation depth ranges obtained from post-event field surveys.

4 Discussion

The comprehensive post-event investigation of Typhoon Hato provides valuable insights into storm surge inundation processes in one of China's most densely urbanized coastal regions. By integrating field reconnaissance, RTK measurements, inundation tracing, floating debris surveys, eyewitness interviews, and numerical model validation, this study establishes a reliable dataset for understanding storm surge characteristics and evaluating hydrodynamic model performance. Such comprehensive field observations complement numerical simulations and provide valuable evidence for improving coastal flood risk assessment.

A major finding of this study is the pronounced spatial variability of storm surge inundation across Guangdong Province. Although all surveyed areas were affected by the same typhoon, inundation intensity varied considerably among different coastal cities. This variability reflects the combined influences of typhoon characteristics, estuarine geomorphology, astronomical tides, local topography, and regional exposure rather than typhoon intensity alone. The most severe inundation occurred in Zhuhai, where landfall near the Pearl River Estuary coincided with elevated astronomical tide. The funnel-shaped estuary and strong onshore winds further amplified storm surge propagation, whereas areas farther from the landfall location or with different coastal configurations experienced substantially lower inundation depths (Yang et al., 2019). These findings demonstrate the importance of local coastal characteristics in controlling storm surge hazards.

The favorable consistency between observed and simulated water levels, as well as field-surveyed and simulated inundation characteristics in terms of spatial extent and water depth, demonstrates the reliability of the numerical model and highlights the value of post-event field surveys as benchmark datasets for numerical model validation. Compared with conventional point-based validation, the integrated framework combining spatially distributed simulation outputs with field inundation data enables a more comprehensive evaluation of model performance. Despite the overall good agreement, notable discrepancies remain in several local areas. Such discrepancies may stem from several sources of uncertainty. First, uncertainties in rainfall, river discharge, and boundary conditions can affect the timing and magnitude of pluvial and fluvial flooding. Uncertainties in topographic and bathymetric data may further modify local flow pathways and determine whether low-lying areas are inundated. Second, model parameterization and land-surface representation can introduce additional discrepancies, as simplified hydraulic parameters and incomplete representations of buildings and drainage infrastructure may not fully resolve local flow processes. Third, coastal defense structures may contribute substantially to spatially heterogeneous discrepancies. Seawalls and coastal dikes can restrict, redirect, or confine floodwaters, thereby locally controlling whether water propagates inland or remains within the coastal zone. Consequently, differences between their actual and modelled crest elevations, structural continuity, openings, and conditions may shift the simulated inundation boundary. Groins can likewise alter nearshore flow patterns and water-level distributions, thereby affecting the pathways through which coastal floodwaters reach adjacent shorelines. Because such structures are often much smaller than the spatial resolution of regional hydrodynamic models, their hydraulic effects may not be adequately resolved. Fourth, the wetting–drying threshold can influence the identification of marginally inundated cells, particularly near the simulated flood boundary. Finally, uncertainties in field observations may also contribute to the observed–simulated discrepancies, owing to incomplete spatial coverage and the

difficulty of accurately delineating inundation boundaries after floodwaters have receded. Notwithstanding these local discrepancies, the integrated validation results verify that the numerical model reliably reproduces the overall spatial distribution and severity of inundation induced by Typhoon Hato. The synergistic combination of validated field observations and numerical simulations improves the credibility of hydrodynamic model applications for coastal flood hazard assessment.

The results also have important implications for coastal flood risk management. As sea level rise and climate change are expected to increase the severity of future storm surge hazards, reliable field observations will remain essential for improving numerical prediction and supporting coastal flood risk assessment. The substantial spatial variability observed in this study further highlights the need for region-specific disaster prevention and emergency management strategies rather than uniform mitigation measures. Importantly, the observed spatial heterogeneity in inundation severity also points to the role of local vulnerability and protection capacity in shaping disaster impacts. During Typhoon Hato, several areas across the Pearl River Delta experienced levee breaches, overtopping, and piping. These failures resulted in prolonged and widespread inundation, affecting a wide range of exposed assets, including agricultural land, aquaculture facilities, transportation, communication, and energy infrastructure. Field investigations further revealed that severe inundation in some locations was closely associated with low protection standards, aging and poorly maintained levees, and gaps in coastal defenses. The different inundation modes summarized in Table 8 further illustrate this mechanism. While overflow was the most widespread mode, several locations experienced combined overflow and dike breach or piping, indicating that structural failure of coastal defenses could further intensify flood propagation. These combined failure modes were observed in areas with relatively high inundation depths, such as Yantian District (1.2–2.0 m) and Humen Town (1.2–1.4 m), highlighting the importance of dike integrity in shaping local inundation severity. The impacts of coastal flooding, therefore, are determined not only by the extent and depth of inundation, but also by how effectively local infrastructure can withstand and contain floodwaters. These findings highlight the need to translate spatially heterogeneous inundation characteristics into differentiated disaster risk management strategies. Areas experiencing severe and extensive inundation should be prioritized for disaster risk assessment and zoning, with particular attention to identifying critical defense gaps and vulnerable infrastructure. Existing coastal defenses, including levees, sluice gates, and drainage facilities, should be systematically inspected and evaluated, with reinforcement, upgrading, or reconstruction prioritized according to their protection capacity and local inundation conditions. For areas containing densely populated communities, critical infrastructure, or major economic assets, the identified inundation risks should also be incorporated into local emergency preparedness and response plans, including targeted evacuation and emergency response measures. Such spatially differentiated risk management can help local authorities better prioritize limited disaster prevention resources and strengthen preparedness for future coastal flooding.

However, several limitations should be further addressed. The flood marks may have been altered before the field investigation, introducing uncertainty into the reconstructed inundation characteristics. In addition, the relative contributions of various uncertainty sources to the simulation-observation mismatches were not quantitatively evaluated in this study. Future work will adopt quantitative uncertainty attribution techniques to identify the primary factors controlling model performance, which is expected to further enhance the accuracy and reliability of storm surge inundation simulations.

5 Conclusions

This study investigated the spatial characteristics and damage mechanisms of storm surge inundation induced by Typhoon Hato (2017) in Guangdong Province through the integration of post-event field observations and numerical modelling. The results demonstrate pronounced spatial heterogeneity in inundation severity across the surveyed coastal areas, reflecting the combined effects of coastal hydrodynamic forcing, local topography, estuarine setting, and the capacity of coastal protection systems. The field investigation further identified distinct inundation and dike failure modes, including dike overtopping, breaching, and piping, which contributed to substantial differences in local inundation severity and disaster impacts. Comparison between field observations and numerical simulations showed generally good agreement, supporting the applicability of the hydrodynamic model for reproducing the major inundation characteristics of the Hato event. Overall, the findings highlight that coastal flood impacts are governed not only by hydrodynamic conditions but also by the vulnerability and protection capacity of exposed areas. Integrating post-event field evidence with numerical modelling therefore provides a useful basis for improving the understanding, validation, and assessment of storm surge inundation and coastal disaster risk.

Data availability

The data supporting the findings of this study are available from the corresponding author upon reasonable request according to the research institution policies.

Author contributions

Shi wrote and revised the manuscript, Chen wrote the manuscript, Du conducted the numerical simulation, Jia wrote the manuscript and participated in the field survey, Fang analyzed the storm surge loss data, Zhao participated in the field survey, Liu organized this research and prepared the manuscript with contributions from all co-authors.

Competing interests

The contact author has declared that none of the authors has any competing interests.

Acknowledgements

We would like to thank the journal's editors and reviewers for their valuable suggestions to improve the paper.

Financial support

This research was funded by the National Natural Science Foundation of China (42671101and 42631012).

References

Bösmeier, A. S., Himmelsbach, I., and Seeger, S.: Reliability of flood marks and practical relevance for flood hazard assessment in southwestern Germany, Nat. Hazards Earth Syst. Sci., 22, 2963–2979, https://doi.org/10.5194/nhess-22-2963-2022, 2022.

Cao, Y., Wang, M., Yao, J., Mo, F., Zhu, H., Hu, L., and Zhai, H.: Stereoscopic Monitoring Methods for Flood Disasters Based on ICESat-2 and Sentinel-2 Data, Remote Sensing, 15, 3015, https://doi.org/10.3390/rs15123015, 2023.

Dottori, F., Di Baldassarre, G., and Todini, E.: Detailed data is welcome, but with a pinch of salt: Accuracy, precision, and uncertainty in flood inundation modeling: OPINION, Water Resour. Res., 49, 6079–6085, https://doi.org/10.1002/wrcr.20406, 2013.

Du, H., Fei, K., Wu, J., and Gao, L.: An integrative modelling framework for predicting the compound flood hazards induced by tropical cyclones in an estuarine area, Environmental Modelling & Software, 175, 105996, https://doi.org/10.1016/j.envsoft.2024.105996, 2024a.

Du, H., Fei, K., and Gao, L.: Nonlinear Tide-River-Surge Interactions and Their Impacts on Compound Flooding During Typhoon Hato in the Pearl River Delta, JGR Oceans, 129, e2023JC020673, https://doi.org/10.1029/2023JC020673, 2024b.

Feaster, T. D. and Koenig, T. A.: Field manual for identifying and preserving high-water mark data, U.S. Geological Survey Open-File Report 2017-1105, 67 p., https://doi.org/10.3133/ofr20171105, 2017.

Feehan, C. J., Filbee-Dexter, K., Thomsen, M. S., Wernberg, T., and Miles, T.: Ecosystem damage by increasing tropical cyclones, Commun Earth Environ, 5, 674, https://doi.org/10.1038/s43247-024-01853-2, 2024.

Gharehtoragh, M. A. and Johnson, D. R.: Using surrogate modeling to predict storm surge on evolving landscapes under climate change, npj Nat. Hazards, 1, 33, https://doi.org/10.1038/s44304-024-00032-9, 2024.

Guangdong Provincial Department of Oceans and Fisheries: 2017 Guangdong Province Marine Disaster Bulletin, Guangdong Provincial Department of Oceans and Fisheries, Guangdong, China, 2018 (in Chinese).

Guo, W., Yao, D., Chen, Z., Ding, P., and Ge, J.: Assessment of future flood risk induced by sea level rise and tropical cyclones under global warming in the Xiamen Bay, Fujian, China, Front. Mar. Sci., 10, 1103279, https://doi.org/10.3389/fmars.2023.1103279, 2023.

Jiao, L., Wang, Y., Jiang, D., Liu, Q., Gao, J., and Lv, X.: Numerical Simulation of Storm Surge-Induced Water Level Rise in the Bohai Sea with Adjoint Data Assimilation, Remote Sensing, 17, 2054, https://doi.org/10.3390/rs17122054, 2025.

Khan, S. D. and Basalamah, S.: Multi-Scale and Context-Aware Framework for Flood Segmentation in Post-Disaster High Resolution Aerial Images, Remote Sensing, 15, 2208, https://doi.org/10.3390/rs15082208, 2023.

Koenig, T. A., Bruce, J. L., O'Connor, J. E., McGee, B. D., Holmes, R. R., Jr., Hollins, R., Forbes, B. T., Kohn, M. S., Schellekens, M. F., Martin, Z. W., and Peppler, M. C.: Identifying and preserving high-water mark data, U.S. Geological Survey Techniques and Methods, book 3, chap. A24, 47 p., https://doi.org/10.3133/tm3A24, 2016.

Muis, S., Aerts, J. C. J. H., Á. Antolínez, J. A., Dullaart, J. C., Duong, T. M., Erikson, L., Haarsma, R. J., Apecechea, M. I., Mengel, M., Le Bars, D., O'Neill, A., Ranasinghe, R., Roberts, M. J., Verlaan, M., Ward, P. J., and Yan, K.: Global Projections of Storm Surges Using High-Resolution CMIP6 Climate Models, Earth's Future, 11, e2023EF003479, https://doi.org/10.1029/2023EF003479, 2023.

Passeri, D. L., Bilskie, M. V., Plant, N. G., Long, J. W., and Hagen, S. C.: Dynamic modeling of barrier island response to hurricane storm surge under future sea level rise, Climatic Change, 149, 413–425, https://doi.org/10.1007/s10584-018-2245-8, 2018.

Qiu, J., Liu, B., Yang, F., Wang, X., and He, X.: Quantitative Stress Test of Compound Coastal-Fluvial Floods in China's Pearl River Delta, Earth's Future, 10, e2021EF002638, https://doi.org/10.1029/2021EF002638, 2022.

Shi, X., Liu, S., Yang, S., Liu, Q., Tan, J., and Guo, Z.: Spatial–temporal distribution of storm surge damage in the coastal areas of China, Nat Hazards, 79, 237–247, https://doi.org/10.1007/s11069-015-1838-z, 2015.

Shi, X., Yu, P., Guo, Z., Sun, Z., Chen, F., Wu, X., Cheng, W., and Zeng, J.: Simulation of storm surge inundation under different typhoon intensity scenarios: case study of Pingyang County, China, Nat. Hazards Earth Syst. Sci., 20, 2777–2790, https://doi.org/10.5194/nhess-20-2777-2020, 2020.

Vogt, T., Treu, S., Mengel, M., Frieler, K., and Otto, C.: Modeling surge dynamics improves coastal flood estimates in a global set of tropical cyclones, Commun Earth Environ, 5, 529, https://doi.org/10.1038/s43247-024-01707-x, 2024.

Wang, X., Guo, Y., and Ren, J.: The Coupling Effect of Flood Discharge and Storm Surge on Extreme Flood Stages: A Case Study in the Pearl River Delta, South China, Int J Disaster Risk Sci, 12, 1–15, https://doi.org/10.1007/s13753-021-00355-5, 2021.

Widiyanto, W., Santoso, P. B., Hsiao, S.-C., and Imananta, R. T.: Post-event field survey of 28 September 2018 Sulawesi earthquake and tsunami, Nat. Hazards Earth Syst. Sci., 19, 2781–2794, https://doi.org/10.5194/nhess-19-2781-2019, 2019.

Yang, J., Li, L., Zhao, K., Wang, P., Wang, D., Sou, I. M., Yang, Z., Hu, J., Tang, X., Mok, K. M., and Liu, P. L.: A Comparative Study of Typhoon Hato (2017) and Typhoon Mangkhut (2018)—Their Impacts on Coastal Inundation in Macau, JGR Oceans, 124, 9590–9619, https://doi.org/10.1029/2019JC015249, 2019.

Yuhi, M., Umeda, S., Arita, M., Ninomiya, J., Gokon, H., Arikawa, T., Baba, T., Imamura, F., Kumagai, K., Kure, S., Miyashita, T., Suppasri, A., Kawai, A., Nobuoka, H., Shibayama, T., Koshimura, S., and Mori, N.: Dataset of Post-Event Survey of the 2024 Noto Peninsula Earthquake Tsunami in Japan, Sci Data, 11, 786, https://doi.org/10.1038/s41597-024-03619-z, 2024.

Zhang, J., Xu, W., Xu, D., Xu, B., Liang, C., Deng, J., and Zhou, P.: Analysis and Evaluation of the Impact of Sea-Level Rise on Storm Surges in the Guangdong–Hong Kong–Macao Greater Bay Area, JMSE, 14, 330, https://doi.org/10.3390/jmse14040330, 2026.

Zhang, Y. and Zhang, T.: A Comprehensive Review of Assessing Storm Surge Disasters: From Traditional Statistical Methods to Artificial Intelligence-Based Techniques, Atmosphere, 15, 359, https://doi.org/10.3390/atmos15030359, 2024.